Supporting information for

Upcycling waste polypropylene separator into carbon nanotube for efficient interfacial solar-driven evaporation and hydroelectric power generation

Mengjie Xu [a,b], Huiyue Wang [b], Xueying Wen [b], Huajian Liu [b], Guixin Hu [b], Qianyu Wei [b], Ran Niu *[,b], Ruikun Pan *[,a], Hui Zhang *[,c], and Jiang Gong*[,b,c]

[a] Ministry of Education Key Laboratory for the Green Preparation and Application of Functional Materials, Hubei Key Laboratory of Polymer Materials, School of Materials Science and Engineering, Hubei University, Wuhan 430062, P. R. China.

[b] Key Laboratory of Material Chemistry for Energy Conversion and Storage, Ministry of Education, Hubei Key Laboratory of Material Chemistry and Service Failure, Hubei Engineering Research Center for Biomaterials and Medical Protective Materials, Semiconductor Chemistry Center, School of Chemistry and Chemical Engineering, Huazhong University of Science and Technology, Wuhan 430074, P. R. China.

[c] Zhongxing Innovative Material Technologies Co. Ltd., Shenzhen 518120, P. R. China.

*Corresponding authors.

E-mail addresses: niuran@hust.edu.cn (R. Niu); rkpan@hubu.edu.cn (R. Pan); zhang.hui@zimt.com.cn (H. Zhang); gongjiang@hust.edu.cn (J. Gong)

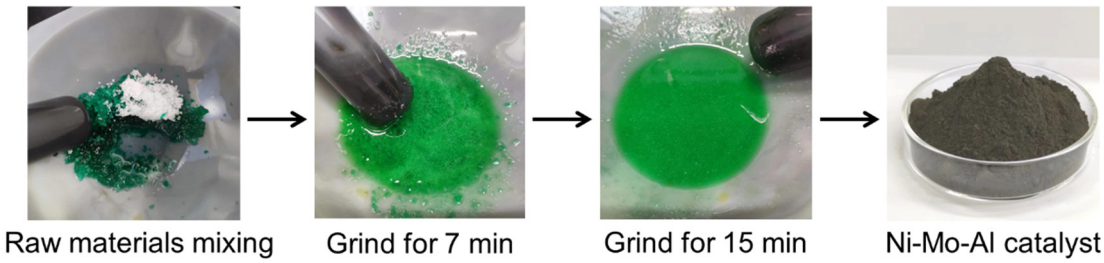

Fig. S1 Photographs showing the preparation process of Ni-Mo-Al catalyst.

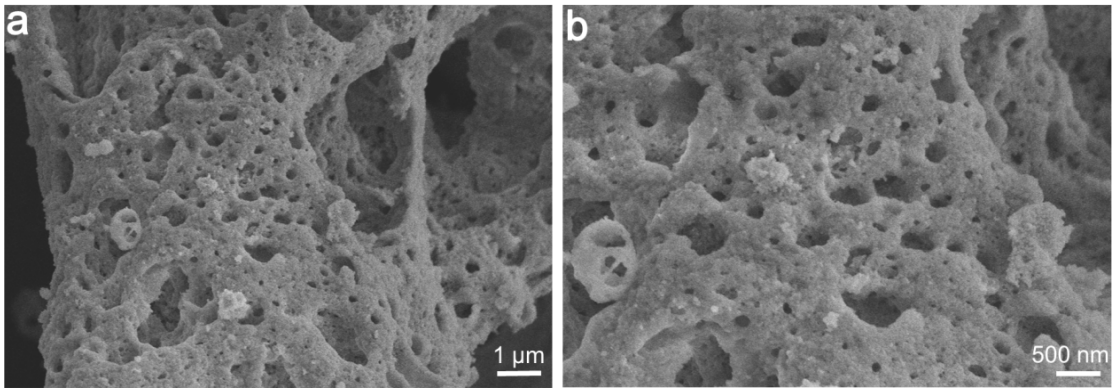

Fig. S2 (a and d) SEM images of Ni-Mo-Al 5-0.1-1 catalyst in different magnifications.

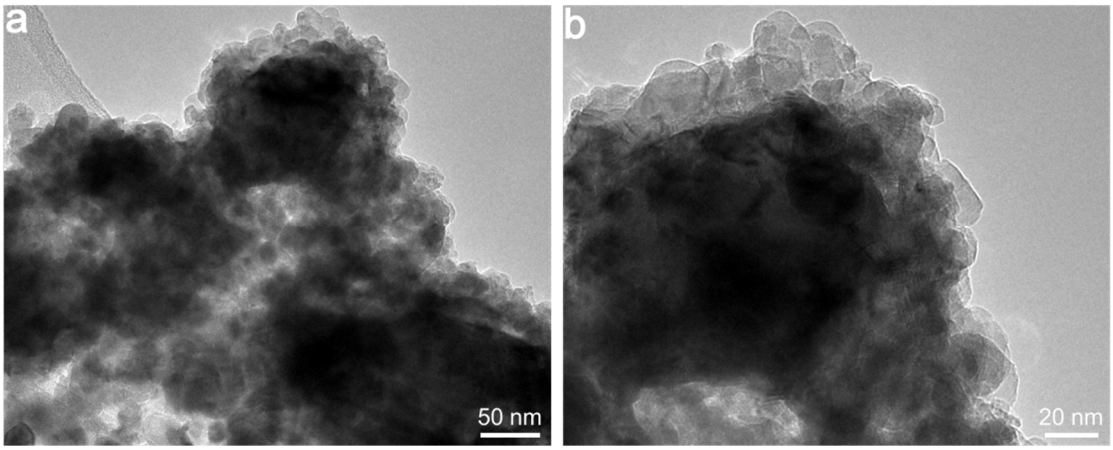

Fig. S3 (a and b) TEM images of Ni-Mo-Al 5-0.1-1 catalyst in different magnifications.

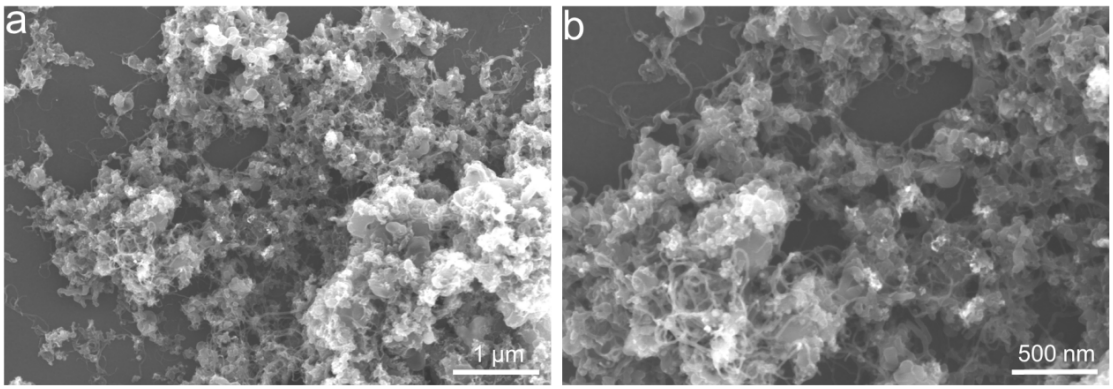

Fig. S4 (a and b) SEM images of CNT-5-0-1 in different magnifications.

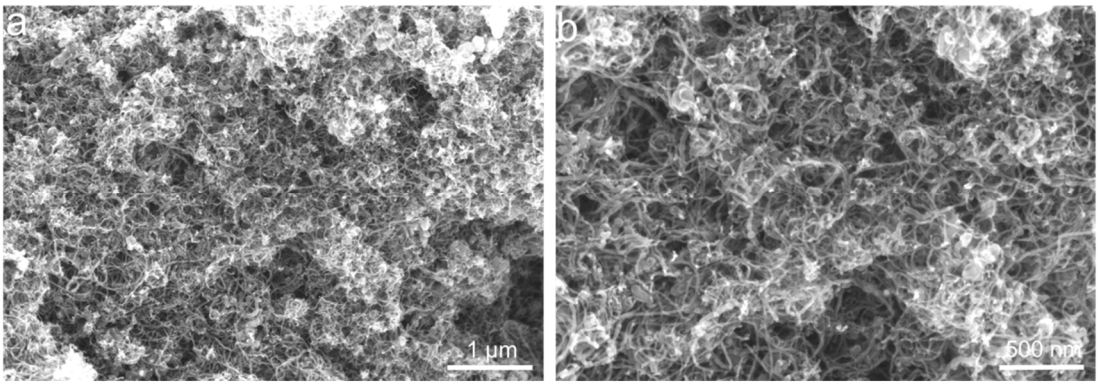

Fig. S5 (a and b) SEM images of CNT-5-0.1-1 in different magnifications.

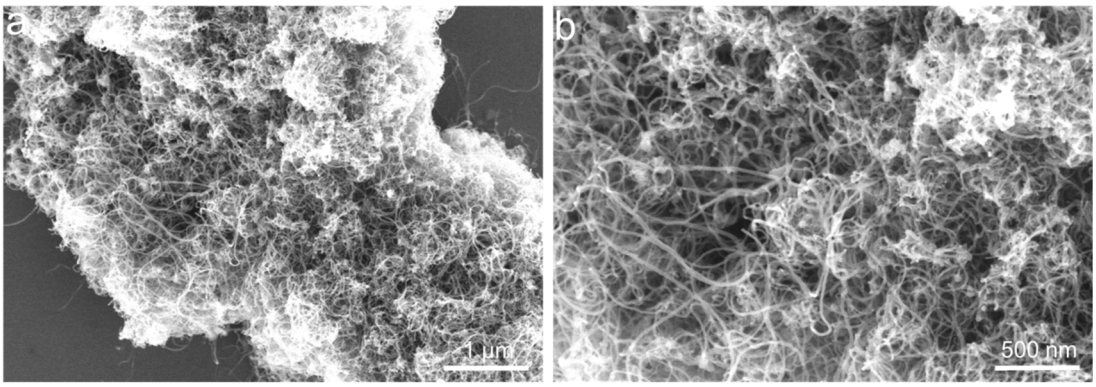

Fig. S6 (a and b) SEM images of CNT-5-1-1 in different magnifications.

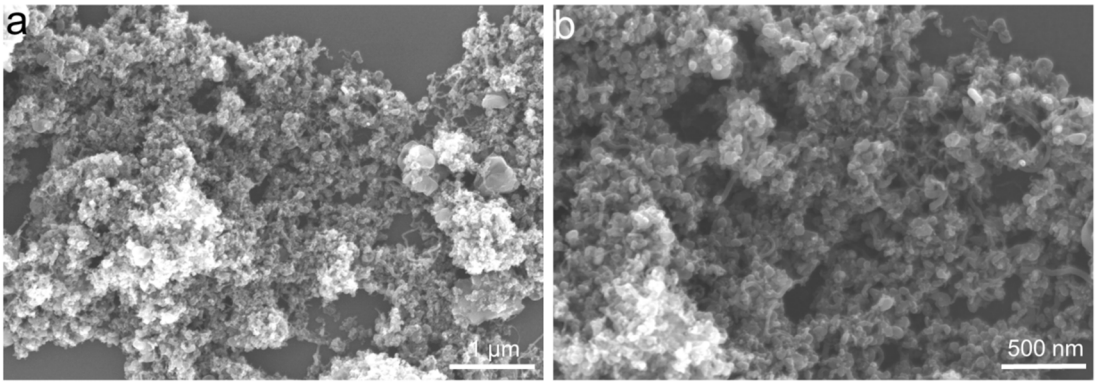

Fig. S7 (a and b) SEM images of CNT-5-0.1-0 in different magnifications.

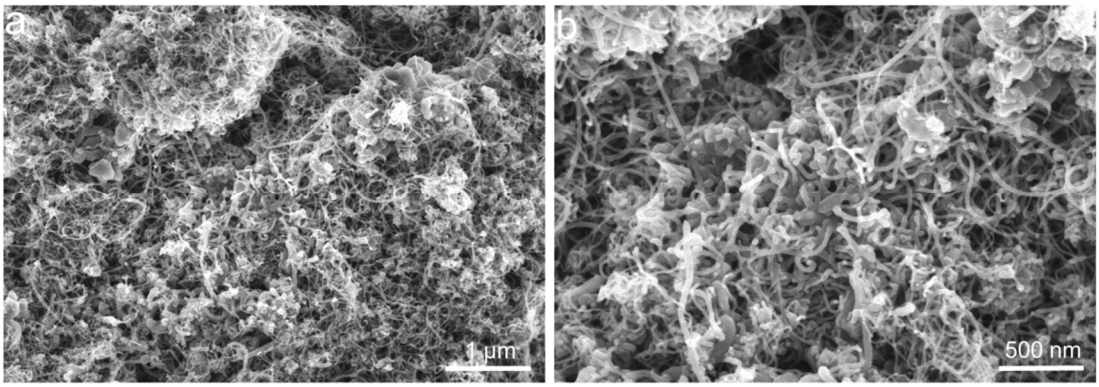

Fig. S8 (a and b) SEM images of CNT-5-0.1-3 in different magnifications.

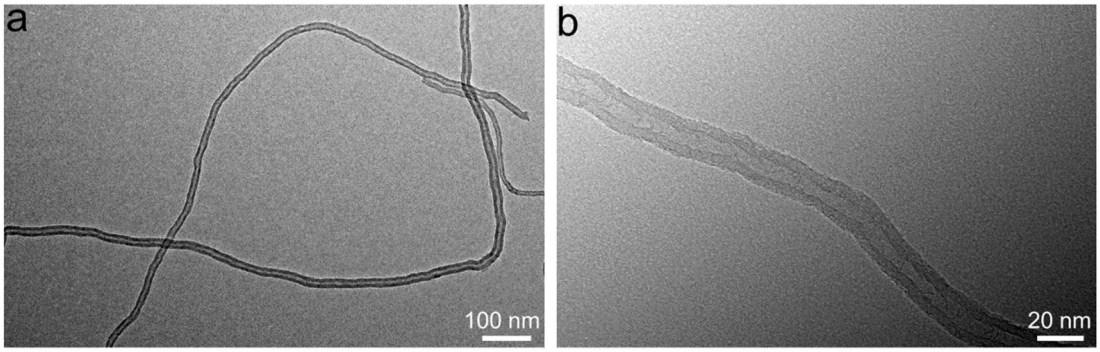

Fig. S9 (a and b) TEM images of CNT-5-0.1-1 in different magnifications.

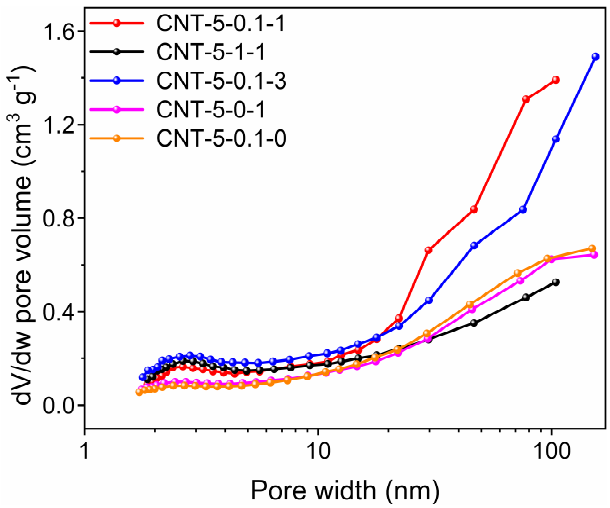

Fig. S10 The pore size distribution plots of CNT-*x* using BJH model.

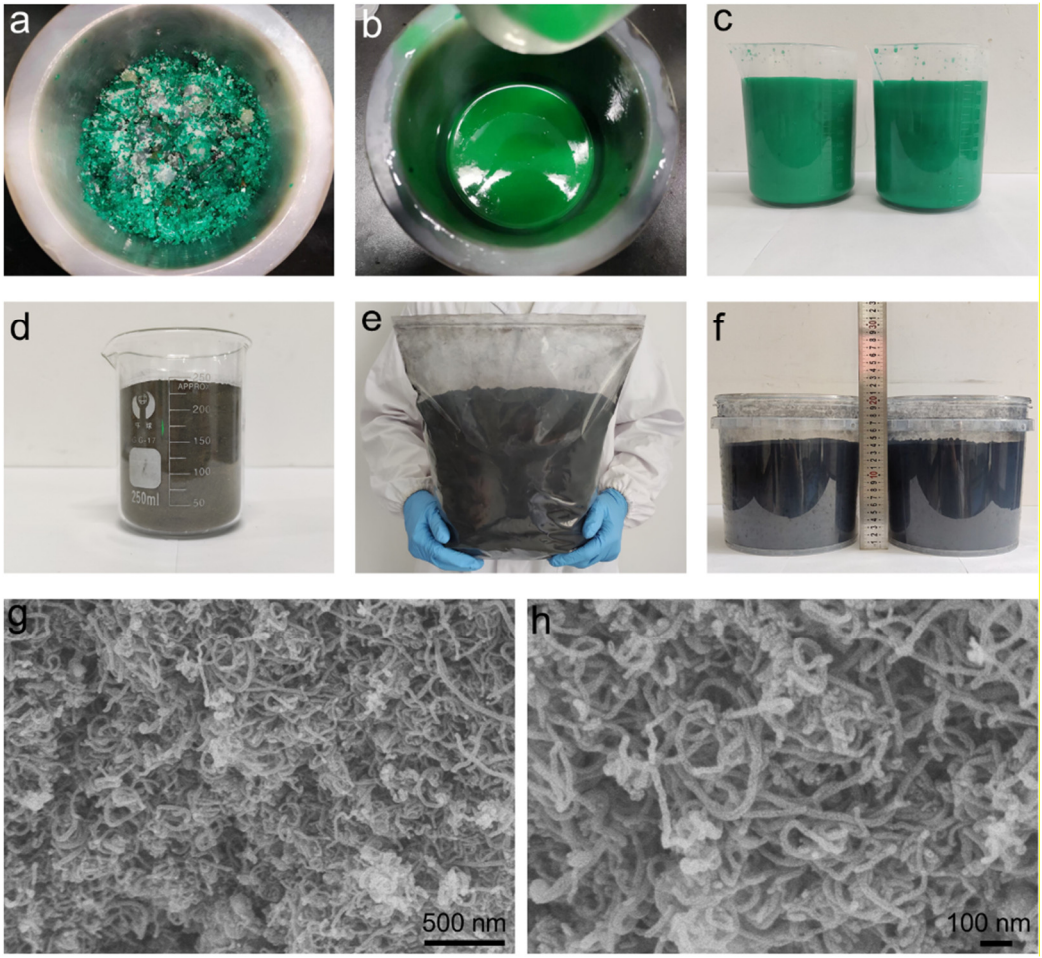

Fig. S11 Photographs of the mixture of catalyst precursors for the Ni-Mo-Al=5-0.1-1 catalyst (a) before or (b and c) after ball milling. (d) Photographs of the Ni-Mo-Al=5-0.1-1 catalyst (115 g) after the heat treatment. (e and f) Photographs and (g and h) of CNT (810 g) from the carbonization of PP using the Ni-Mo-Al=5-0.1-1 catalyst.

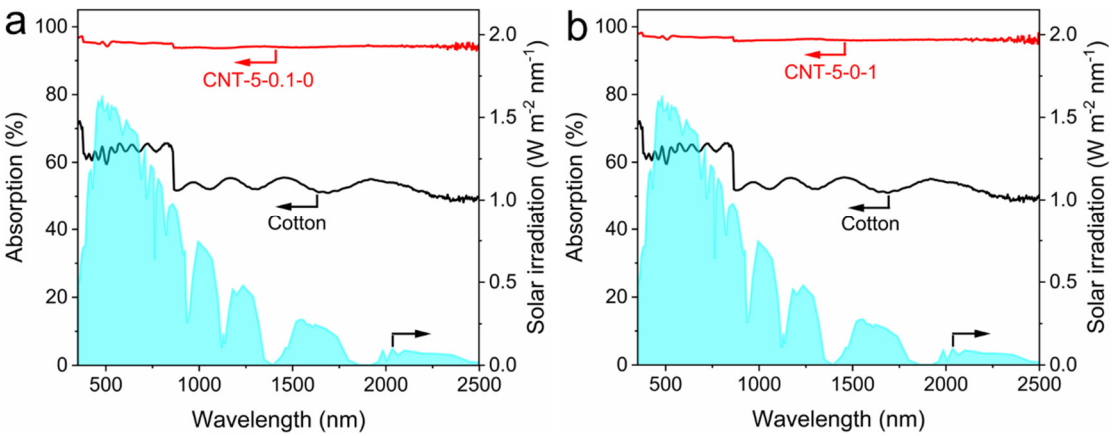

Fig. S12 UV-Vis-NIR absorption spectra of (a) CNT-5-0.1-0 and (b) CNT-5-0-1.

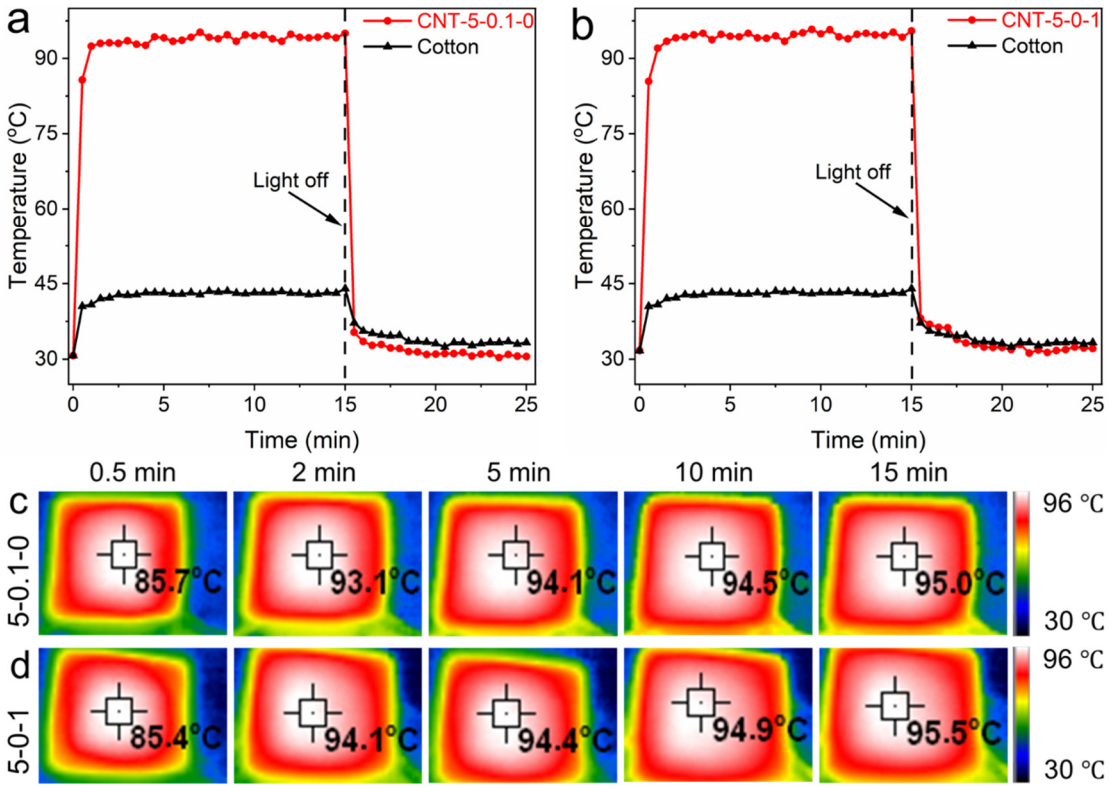

Fig. S13 (a and c) Surface temperature curves and (b and d) infrared images of CNT-5-0.1-0 and CNT-5-0-1 evaporators under 1 Sun irradiation.

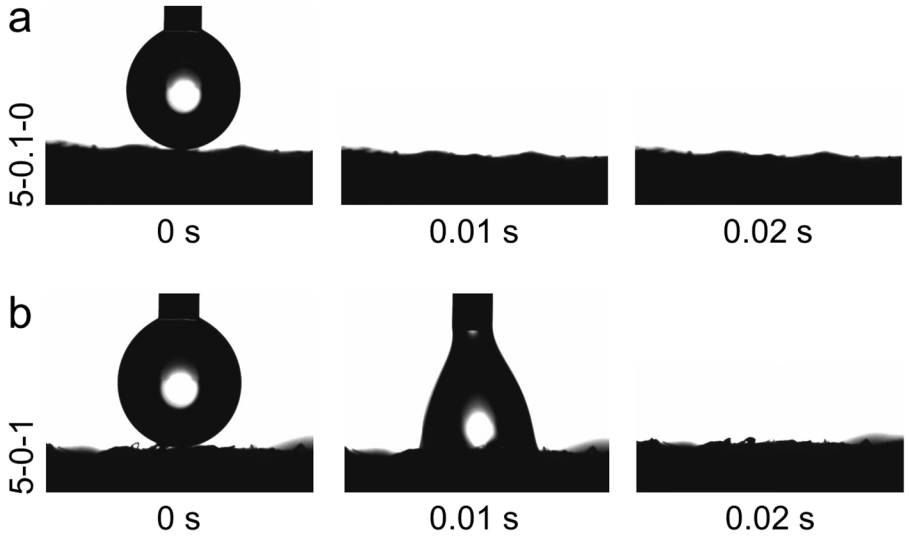

Fig. S14 Time evolution for contact angles of (a) CNT-5-0.1-0, and (b) CNT-5-0-1.

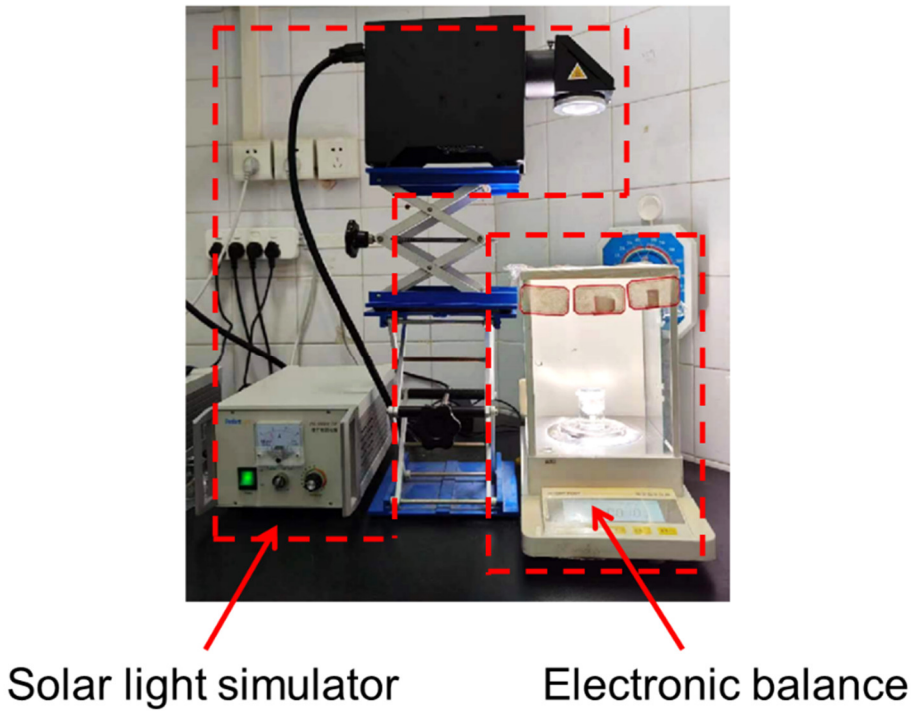

Fig. S15 Photograph of the interfacial solar steam generation system in this work.

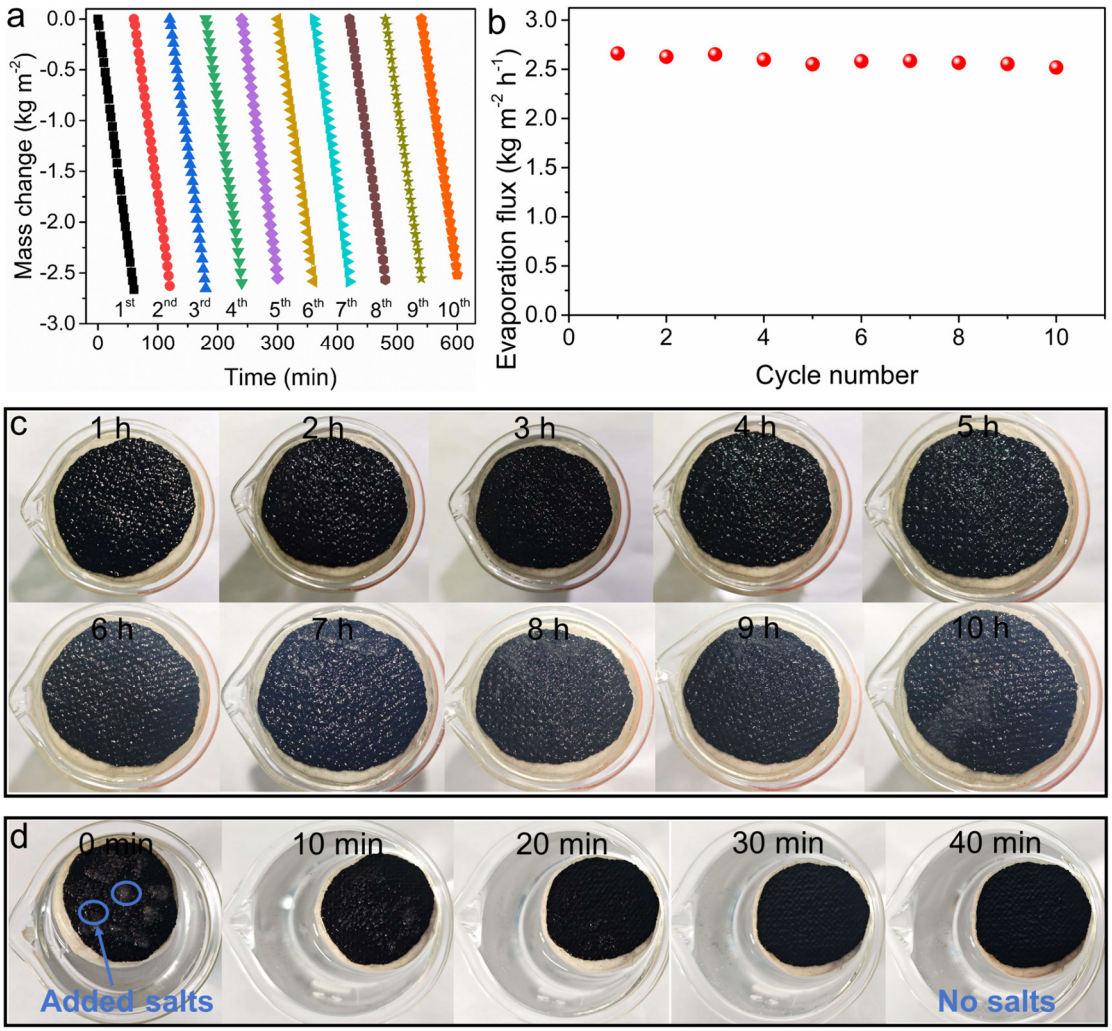

Fig. S16 (a) Water mass change and (b) evaporation flux of the CNT-5-0.1-1 evaporator in seawater for 10 cycles (1 h for one cycle). (c) Digital images of the CNT-5-0.1-1 evaporator during 10 cycles. (d) Photographs of salt ablation process on the surface of the CNT-5-0.1-1 evaporator.

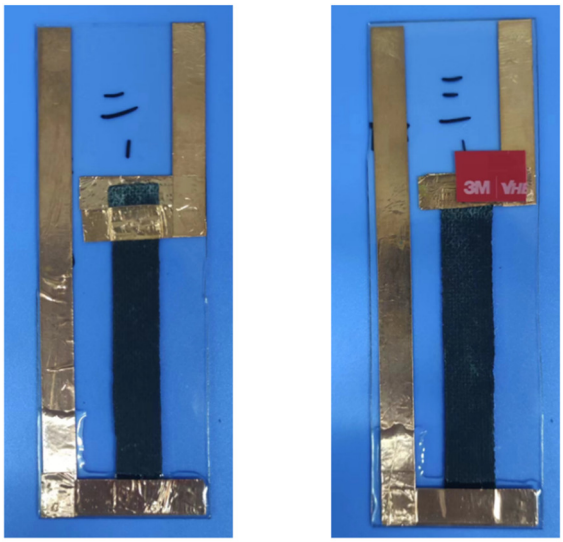

Fig. S17 Photographs of the CNT-*x* device for electricity generation.

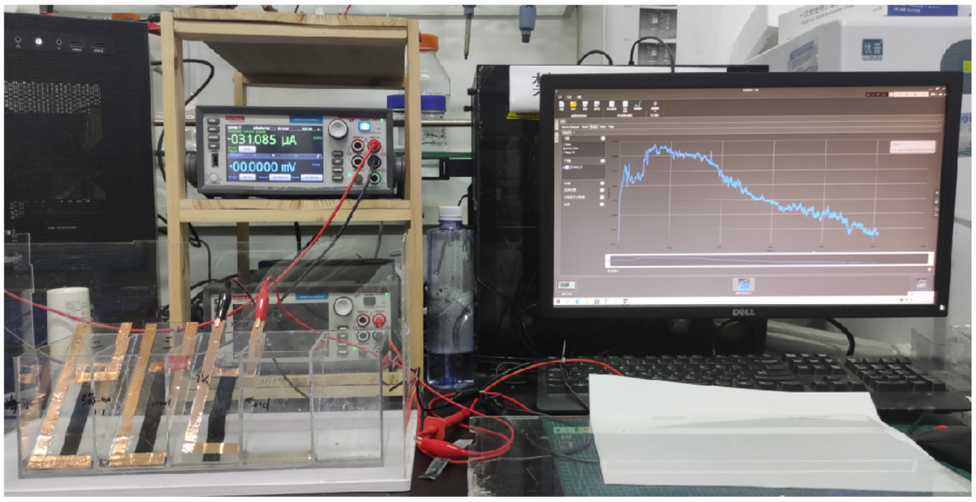

Fig. S18 Overall diagram of water evaporation power generation in real time.

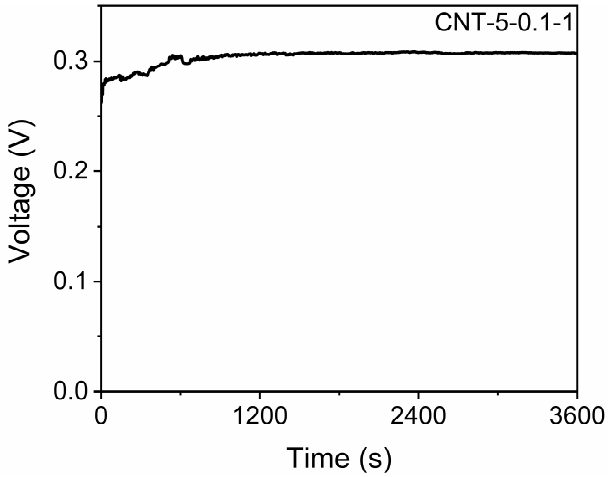

Fig. S19 Open-circuit voltage of the CNT-5-0.1-1 device in seawater.

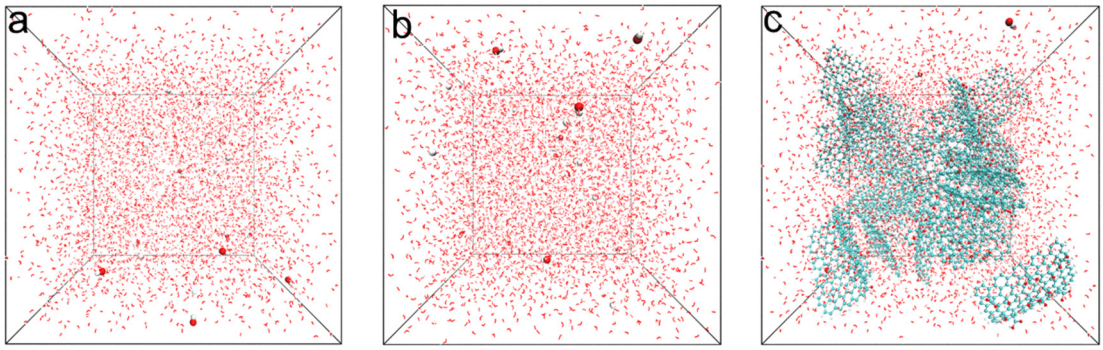

Fig. S20 Snapshot of MD simulations of (a) initial-state results with pure water, (b) end-state results with pure water, and (c) initial-state results with graphene nanosheet, H^+, OH^-, and pure water.

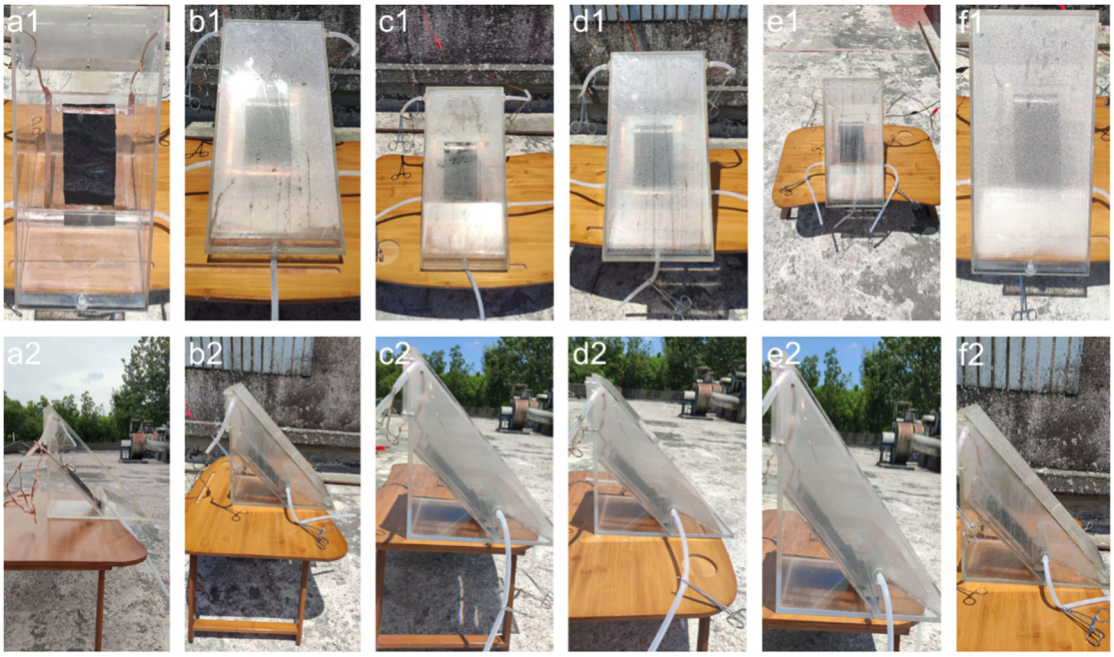

Fig. S21 Photographs of water evaporation and power generation in outdoor experiment at different daytime: (a1 and a2) 0 h, (b1 and b2) 1 h, (c1 and c2) 2 h, (d1 and d2) 3 h, (e1 and e2) 4 h, and (f1 and f2) 5 h.

Table S1 XPS analysis result of CNT-5-0.1-1.

Element	C	O	Ni	Mo	Al
Content (%)	91.76	8.13	0.02	0.03	0.06

Table S2 Comparison of the interfacial solar steam generation performance of CNT-5-0.1-1 evaporator with some recently reported photothermal materials under 1 kW m^{-2} irradiation.

Entry	Photothermal material	Evaporation flux (kg m^{-2} h^{-1})	Efficiency (%)	Reference in SI
1	CNT-5-0.1-1 evaporator	2.85	98.9	This work
2	CCN evaporator	2.70	98.6	[1]
3	Kapok fiber/MXene constructed hydrogel	2.49	91.5	[2]
4	ZCP-20	2.48	67.1	[3]
5	MnO/C-600 membrane	2.38	98.4	[4]
6	CSL-C@MXene-20 mg	2.35	88.2	[5]
7	CMS-*x* aerogel	2.34	91.7	[6]
8	Bi-MOF	2.16	87.5	[7]
9	MCP sponge-based evaporator	2.04	85	[8]
10	PPy sponge	1.89	85.6	[9]
11	GCP-20	1.87	79.2	[10]
12	CDW@MOF	1.81	89	[11]
13	MT-Ag_2S/CAM	1.80	91.6	[12]
14	CCS STE	1.58	82	[13]
15	Ag/$MgFe_2O_4$@SCW	1.55	88.6	[14]
16	CCMs-*x* SVD	1.41	90.8	[15]
17	SA-H@CP	1.36	85	[16]
18	Janus fabric evaporator	1.17	78	[17]

Table S3 Summary of the enthalpy values measured from dark experiment and DSC measurement.

Enthalpy (kJ g^{-1})	Pure water	Cotton cloth	CNT-5-0.1-1 evaporator	CNT-5-0.1-0 evaporator	CNT-5-0-1 evaporator
Dark experiment	2.434	2.314	1.677	1.887	1.787
DSC measurement	2.301	2.051	1.541	1.886	1.796

Table S4 Comparison of V_{OC} and evaporation flux with some recently reported materials.

Entry	Material	Voltage (mV)	Evaporation flux (kg m^{-2} h^{-1})	Reference in SI
1	CNT-5-0.1-1 device	350	2.79	This work
2	CHN-CB	460	2.1	[18]
3	Chiber@CNT/rGO	260	2.1	[19]
4	CNT modified wood	250	1.19	[20]
5	PCP-600 device	212	2.74	[21]
6	PCC-800	201	2.49	[22]
7	Thermo-electrochemical cell	200	1.10	[23]
8	Carbon cloth	141	1.48	[24]
9	Nb_4N_5 nanosheet	135	2.30	[25]
10	Carbon fiber	117	1.33	[26]
11	CNTs/carbon fiber foam	105	1.67	[27]
12	CNTP	100	1.28	[28]
13	MoS_2-*x* NSA	98.2	1.32	[29]
14	DDPA-PDN	83	1.07	[30]

15	CNTs/nafion	66	1.1	[31]
16	CNTs/cellulose sponge	60	1.20	[32]

Note S1 Calculation of evaporation flux and conversion efficiency

The interfacial solar-powered steam generation system consisting of a solar light simulator (PLS-SXE300E), a UV-enhanced total reflection filter as a light source, and an electronic balance (JA2003) for real-time and accurate measurement of changes in water quality. The surrounding temperature and relative humidity were approximately 38 ℃ and 33%, respectively. An infrared camera (DMI220) was used to collect photos of the surface temperature and thermal distribution of evaporators. Evaporation rate (m, kg m^{-2} h^{-1}) and conversion efficiency (η, %) of the evaporator were calculated through Equations S1 and S2, respectively,

$$m = \Delta m / (S \times t) \quad \text{(S1)}$$

$$\eta = m' \times h_{LV} / (3600 \times P_{in}) \quad \text{(S2)}$$

where Δm stands for the water mass loss in 1 h (kg), S represents the lighting area of the evaporator (6.15×10^{-4} m^2), t refers to the irradiation time (1 h), m' presents the evaporation flux that subtracts the darkroom evaporation flux, h_{LV} represents the water evaporation enthalpy (kJ kg^{-1}), and P_{in} stands for the illumination intensity (1 kW m^{-2}). Note: We could adjust the current density of the solar simulator and/or the distance between simulated sunlight emitter and the surface of evaporators to change the irradiation intensity.

Note S2 Characterization

Scanning electron microscopy (SEM, SU8010) and high-resolution transmission electron microscope (HRTEM, Tecnai G2 F30) was used to investigate the morphology and microstructure. Analysis of the crystal structure of materials by means of X-ray diffraction (XRD, SmartLab-SE). The degree of graphitization had been analyzed by means of a laser confocal Raman spectroscopy (LabRAM HR800). The thermal

stability of CNT-5-0.1-1 was measured by thermal gravimetric analysis (TGA) under air flow using a TA Instruments SDT Q600. The surface analyzer (Micromeritics ASAP 2460) measured the specific surface area and pore structure of. The pre-heating temperature and time of the sample were 80 °C and 12 h, respectively. The density functional theory (DFT) model or Barret-Joyner-Halenda (BJH) model was used to determine the distribution of pore sizes. Generally, the pore can be divided into three types, that is, micropore (< 2 nm), mesopore (2-50 nm) and macropore (> 50 nm). The functional group of CNT-5-0.1-1 was analyzed by Fourier-transform infrared spectroscopy (FT-IR, BRUKER Vertex 80). X-ray photoelectron spectroscopy (XPS) was conducted using the Thermo ESCALAB 250XI (Japan) instrument. Light absorption was tested via UV-Vis-NIR spectrophotometer (Lambda 750 S) within the spectral range of 300–2500 cm^{-1}. The micro-optical contact angle measurement instrument (Dataphysics OCA15EC) was used to measure the contact angle of water. Thermal conductivity was tested by a thermal conductivity analyzer (Hot Disk, TPS 2500). Differential scanning calorimeter (DSC) was conducted at DSC2500. The surface temperature distribution was examined using the COMSOL Multiphysics 5.6 software. Keithley 2450 electrometer was used for testing open-circuit voltage and short-circuit current. The ambient temperature and relative humidity were approximately 28 ℃ and 33%, respectively.

Note S3 COMSOL simulation

The simulated 3D models were established based on the actual CNT-5-0.1-1 membrane evaporation system, which mainly consisted of CNT-5-0.1-1 membrane, PS foam, and bulk water. The upper hollow cylinder with 2 mm in height and 15 mm in radius was simulated to the membrane evaporator, the middle core cylinder with 3 mm in height and 15 mm in radius was simulated to the floating PS foam, and the remainder of a whole cylinder with 40 mm in height and 15 mm in radius was simulated to the bulk water. Subsequently, the temperature distribution was described as the following equations,

$$E_{in} = \rho C_{\mathrm{p}} \frac{\partial \mathrm{T}}{\partial \mathrm{t}} + \rho C_{\mathrm{p}} \boldsymbol{u} \cdot \nabla T + \nabla \cdot \boldsymbol{q} \quad (\mathbf{S3})$$

$$\boldsymbol{q} = -\boldsymbol{k} \nabla \boldsymbol{T} \quad (\mathbf{S4})$$

where $\boldsymbol{E_{in}}$ is the thermal energy input from the solar irradiation; $\boldsymbol{T}$ (x, t) refers to the local temperature; x and t are the space vector and time, respectively; $\boldsymbol{\rho}$, $\boldsymbol{C_{\mathrm{p}}}$ and $\boldsymbol{k}$ are the mass density, specific thermal capacity, and thermal conductivity of the matters, respectively; $\boldsymbol{u}$ is the fluid flow speed of the aqueous medium.

The theoretical simulation was performed by COMSOL Multiphysics 5.6 under the steady-state analysis mode. The environment temperature was set to 298.15 K, and the heat convection between the upper surface of evaporator and air was corrected by Newton's law of cooling. The thermal conductivity, density, and specific thermal capacity of cotton cloth are 0.0674 W m^{-1} K^{-1}, 67 kg m^{-3}, and 4025.43 J kg^{-1} K^{-1}, respectively. The thermal conductivity, density, and specific thermal capacity of CNT-5-0.1-1 membrane are 0.0752 W m^{-1} K^{-1}, 101 kg m^{-3}, and 3703.95 J kg^{-1} K^{-1}, respectively. The thermal conductivity, density, and specific thermal capacity of PS foam are 0.03 W m^{-1} K^{-1}, 30 kg m^{-3}, and 1300 J kg^{-1} K^{-1}, respectively.

Note S4 Analyses of heat loss

Normally, the heat loss of water evaporation process includes radiation, convection, and conduction. The details of calculating Heat Loss are shown as follows:

(1) Radiation

The heat radiation loss was calculated by the Stefan-Boltzmann equation,

$$\emptyset = \boldsymbol{\varepsilon A \sigma} (\boldsymbol{T_1^4} - \boldsymbol{T_2^4}) \quad (\mathbf{S5})$$

where $\emptyset$ represents the heat flux, $\boldsymbol{\varepsilon}$ is the emissivity, and the emissivity in the water evaporation processes is supposed to have a maximum emissivity of 1. $\boldsymbol{A}$ is the effective evaporation surface area (6.16×10^{-4} m^2). $\boldsymbol{\sigma}$ is the Stefan-Boltzmann constant (the value is 5.67×10^{-8} W m^{-2} K^{-4}). $\boldsymbol{T_1}$ is the surface temperature of the as-prepared materials after stable steam generation under one-sun illumination (ca. 52.1 °C, 325.25 K), and $\boldsymbol{T_2}$ is the ambient temperature upward of the absorber (ca. 38.5 °C, 311.65 K). Then using the following equation to calculate the radiation loss,

$$\eta_{rad} = \emptyset / P_{in} \quad (S6)$$

Therefore, the calculated heat radiation loss of CNT-5-0.1-1 evaporator is 6.2%.

(2) Convection

The convective heat loss is defined by Newton's law of cooling as shown below,

$$Q = hA\Delta T \quad (S7)$$

where Q is the convection heat flux, h represents the convection heat transfer coefficient, which is approximately 5 W m^{-2} K^{-1}. ΔT is the difference between the surface temperature of CNT-5-0.1-1 evaporator and the ambient temperature upward the absorber. Consequently, the connection heat loss of CNT-5-0.1-1 evaporator was calculated through Equation S7, and the value is 4.2%.

(3) Conduction

$$Q = Cm\Delta T \quad (S8)$$

where Q is the heat energy, C presents the specific heat capacity of water (4.2 kJ K^{-1} kg^{-1}), and m denotes the weight of water (g). ΔT is the increased temperature of water. In this work, m = 35 g, ΔT = 0.5 K, Consequently, according to Equation S8, the calculated conduction heat loss of CNT-5-0.1-1 evaporator is ca. 3.3%.

Therefore, the heat loss of PCP-700 evaporator in the water evaporation is ca. 13.7%.

Note S5 Calculation of water evaporation enthalpy

The energy for water to evaporate in dark is gained from the environment, which is therefore the same for different evaporators based on previous work.

Considering theoretical evaporation enthalpy of liquid water is ca. 2.434 kJ g^{-1}. Then enthalpy values are obtained as follows,

$$U_{in} = E_{aque} m_g = E_0 m_0 \quad (S9)$$

where U_{in} is the total energy absorbed from the environment per hour; E_0 and m_0 refer to the water vaporization enthalpy (2.43 kJ g^{-1}) and the water mass loss (g) of pure water without evaporators in the dark, respectively; E_{aque} is the equivalent

evaporation enthalpy of the corresponding system (kJ g^{-1}), and $\boldsymbol{m_g}$ means the corresponding water mass change.

The mass loss of pure water (Water), cotton cloth, CNT-5-0.1-1, CNT-5-0.1-0, and CNT-5-0-1 evaporators in the dark is 290, 305, 421, 374, and 395 mg, respectively. Therefore, the water evaporation enthalpy of cotton cloth, CNT-5-0.1-1, CNT-5-0.1-0, and CNT-5-0-1 is 2.041, 1.486, 1.601 and 1.651 kJ g^{-1}, respectively, which is reduced by 5%, 31%, 22% and 27% in comparison to pure water (2.434 kJ g^{-1}), respectively.

Note S6 Theoretical calculation

The size of carbon oxide nanotubes synthesized in the experiment is too large, and single-side oxidized graphene fragments are used to falsely oxidize carbon nanotubes in the simulation calculation. The partial charge of graphene oxide with different oxygen content (graphene nanosheet, CNT) was calculated using Gaussian 16 code [33] and the 6-311g(d,p) basis functions were applied [34]. The OPLSS-AA force field [35] and Auxiliary Tools of Force Field (AuToFF) were used to parametrize all atoms, such as the bond parameters, angle parameters and the dihedral angles, and so on.

The interactions of different graphene oxide with H^+ and OH^- ions were studied by molecular dynamics (MD) simulation. In system 1, 30 graphene nanosheet molecules, 10 H^+ ions, 10 OH^- ions and 5560 water molecules were randomly inserted into a cube box with a side length of 7.0 nm. The model of water molecule is TIP_3P [36]. The MD simulations were performed in the GROMACS 2021 software package [37-39]. The steepest descent method was applied to minimize the initial energy for each system with a force tolerance of 1 kJ/ (mol^{-1} nm^{-1}) and a maximum step size of 0.002 ps before MD calculations [40]. In all the three directions, periodic boundary conditions were imposed. Leapfrog algorithm was used to integrate the Newtonian equation of motion [40]. The MD simulation was processed in an NPT ensemble and the simulation time is 20 ns.

In NPT simulations, the pressure was maintained at 1 bar by the Berendsen barostat in an isotropic manner [41]. The temperature was maintained by the V-rescale thermostat at 298.15 K. The LINCS algorithm [42] was performed for constrain bond lengths of

hydrogen atoms. A cutoff of 1.0 nm was employed to calculate the short-range van der Waals interactions and the electrostatic interactions [43].

References in Supporting Information

1. J. Liu, Z. Fan, H. Liu, L. Liu, X. Wen, H. Wang, R. Niu, H. Wang, J. Cheng and J. Gong, *Journal of Environmental Chemical Engineering*, 2024, **12**, 112363.
2. Q. Su, Z. Wu, X. Huang, J. Yan, L. Tang, H. Xue and J. Gao, *International Journal of Biological Macromolecules*, 2024, **260**, 129403.
3. Y. Zhu, H. Lan, P. He, X. Zhu, J. Gong, Z. Dong and M. Zeng, *Materials Advances*, 2023, **4**, 1628-1636.
4. Z. Fan, J. Ren, H. Bai, P. He, L. Hao, N. Liu, B. Chen, R. Niu and J. Gong, *Chemical Engineering Journal*, 2023, **451**, 138534.
5. G. Zhang, Y. Zhang and J. Jiang, *Separation and Purification Technology*, 2024, **347**, 127588.
6. C. Zhang, Y. Wang, Q. Liu, Y. Chen, S. Zhang, Y. Kou, X. Jian and Z. Weng, *Chemical Engineering Journal*, 2024, **489**, 151247.
7. Z. Fan, J. Liu, H. Liu, L. Liu, Y. She, X. Wen, H. Wang, G. Hu, R. Niu and J. Gong, *Journal of Energy Chemistry*, 2024, **94**, 527-540.
8. P. Lu, S. Cheng and S. Guan, *Journal of Environmental Chemical Engineering*, 2024, **12**, 112662.
9. Z. Yu, Y. Su, R. Gu, W. Wu, Y. Li and S. Cheng, *Nano-Micro Letters*, 2023, **15**, 214.
10. J. Han, Z. Dong, L. Hao, J. Gong and Q. Zhao, *Green Energy & Environment*, 2023, **8**, 151-162.
11. S. Jing, Q. Ji, A. Wang, J. Zhao, H. Liang, F. Chen, P. Kannan and P. Tsiakaras, *Applied Thermal Engineering*, 2024, **244**, 122629.
12. X. Bai, Q. Wang, M. Tan, P. Zhang, S. Sun, D. Wu, H. Mei, G. Shan, N. Wang, H. Hao, T. Wang and X. Huang, *Chemical Engineering Journal*, 2024, **489**, 151441.
13. S. Lal, K. Sundhar and S. K. Batabyal, *Solar Energy*, 2024, **270**, 112374.
14. S. Luo, Z. Liu, X. Yin, Z. Lin, S. Zhang, J. Chen and M. Guo, *Small*, 2024, **20**, 2309087.
15. J. Wang, M. Sun, C. Liu, Y. Ye, M. Chen, Z. Zhao, Y. Zhang, X. Wu, K. Wang and Y. Zhou, *Advanced Materials*, 2023, **35**, 2306103.
16. Y. Chen, L. Cheng, Q. Liu, M. Chen, C. Li, L. Wang, J. Shen, P. Senin, S. Yan and

T. Bian, *Applied Surface Science*, 2024, **656**, 159667.

17. C. Gao, B. Zhou, J. Li, Y. Chen, Q. Wang, J. Mao and J. Guo, *Chemical Engineering Journal*, 2023, **463**, 142002.
18. H. He, X.-M. Song, M. Huang, X. Hou, Z. Song and Y. Zhang, *Green Chemistry*, 2023, **25**, 9343-9350.
19. Y. Wu, J. Ma, S. Zang, W. Zhou, Z. Wang, M. Han, S. M. Osman, C. Wang, Y. Yamauchi, J. You, M. An, L. Wang and Z. Yuan, *Chemical Engineering Journal*, 2023, **472**, 144600.
20. Y. Ding, S. Li, J. Tian, F. Wang, Y. Shi, X. Tao, X. Wang, R. Lei and X. Chen, *ACS Applied Electronic Materials*, 2021, **3**, 5287-5295.
21. H. Liu, L. Liu, Z. Fan, J. Liu, H. Wang, X. Wen, G. Hu, K. Liu, R. Niu and J. Gong, *Chemical Engineering Journal*, 2024, **485**, 149690.
22. B. Chen, J. Ren, Y. Song, P. He, H. Bai, Z. Fan, R. Niu and J. Gong, *ACS Sustainable Chemistry & Engineering*, 2022, **10**, 16427-16439.
23. Q. Shen, Z. Ning, B. Fu, S. Ma, Z. Wang, L. Shu, L. Zhang, X. Wang, J. Xu, P. Tao, C. Song, J. Wu, T. Deng and W. Shang, *Journal of Materials Chemistry A*, 2019, **7**, 6514-6521.
24. Y. Xu, Z. Guo, J. Wang, Z. Chen, J. Yin, Z. Zhang, J. Huang, J. Qian and X. Wang, *ACS Applied Materials & Interfaces*, 2021, **13**, 27129-27139.
25. L. Wang, Y. Ma, G. Yang, X. Li, D. Liu, S. Qin and W. Lei, *Chemical Engineering Journal*, 2023, **472**, 144761.
26. D. Wu, J. Liang, D. Zhang, C. Zhang and H. Zhu, *Solar Energy Materials and Solar Cells*, 2020, **215**, 110591.
27. F. Zhang, Y. Li, H. Cai, Q. Liu and G. Tong, *Carbohydrate Polymers*, 2020, **241**, 116253.
28. Y. Duan, M. Weng, W. Zhang, Y. Qian, Z. Luo and L. Chen, *Energy Conversion and Management*, 2021, **241**, 114306.
29. B. Yuan, L. Yang, H. Yang, L. Bai, W. Wang, D. Wei, Y. Liang and H. Chen, *Energy Conversion and Management*, 2022, **252**, 115070.
30. Y. Cui, J. Liu, Z. Li, M. Ji, M. Zhao, M. Shen, X. Han, T. Jia, C. Li and Y. Wang, *Advanced Functional Materials*, 2021, **31**, 2106247.
31. P. Yang, K. Liu, Q. Chen, J. Li, J. Duan, G. Xue, Z. Xu, W. Xie and J. Zhou, *Energy & Environmental Science*, 2017, **10**, 1923-1927.
32. L. Zhu, T. Ding, M. Gao, C. K. N. Peh and G. W. Ho, *Advanced Energy Materials*,

2019, **9**, 1900250.

33. M. J. Frisch, G. W. Trucks, H. B. Schlegel, G. E. Scuseria, M. A. Robb, J. R. Cheeseman, G. Scalmani, V. Barone, G. A. Petersson, H. Nakatsuji, X. Li, M. Caricato, A. V. Marenich, J. Bloino, B. G. Janesko, R. Gomperts, B. Mennucci, H. P. Hratchian, J. V. Ortiz, A. F. Izmaylov, J. L. Sonnenberg, Williams, F. Ding, F. Lipparini, F. Egidi, J. Goings, B. Peng, A. Petrone, T. Henderson, D. Ranasinghe, V. G. Zakrzewski, J. Gao, N. Rega, G. Zheng, W. Liang, M. Hada, M. Ehara, K. Toyota, R. Fukuda, J. Hasegawa, M. Ishida, T. Nakajima, Y. Honda, O. Kitao, H. Nakai, T. Vreven, K. Throssell, J. A. Montgomery Jr., J. E. Peralta, F. Ogliaro, M. J. Bearpark, J. J. Heyd, E. N. Brothers, K. N. Kudin, V. N. Staroverov, T. A. Keith, R. Kobayashi, J. Normand, K. Raghavachari, A. P. Rendell, J. C. Burant, S. S. Iyengar, J. Tomasi, M. Cossi, J. M. Millam, M. Klene, C. Adamo, R. Cammi, J. W. Ochterski, R. L. Martin, K. Morokuma, O. Farkas, J. B. Foresman and D. J. Fox, *Journal*, 2016.
34. G. A. Petersson and M. A. Al-Laham, *The Journal of Chemical Physics*, 1991, **94**, 6081-6090.
35. W. L. Jorgensen, D. S. Maxwell and J. Tirado-Rives, *Journal of the American Chemical Society*, 1996, **118**, 11225-11236.
36. W. L. Jorgensen, J. Chandrasekhar, J. D. Madura, R. W. Impey and M. L. Klein, *The Journal of Chemical Physics*, 1983, **79**, 926-935.
37. D. Van Der Spoel, E. Lindahl, B. Hess, G. Groenhof, A. E. Mark and H. J. C. Berendsen, *Journal of Computational Chemistry*, 2005, **26**, 1701-1718.
38. M. J. Abraham, T. Murtola, R. Schulz, S. Páll, J. C. Smith, B. Hess and E. Lindahl, *SoftwareX*, 2015, **1-2**, 19-25.
39. H. J. C. Berendsen, D. van der Spoel and R. van Drunen, *Computer Physics Communications*, 1995, **91**, 43-56.
40. W. F. Van Gunsteren and H. J. C. Berendsen, *Molecular Simulation*, 1988, **1**, 173-185.
41. H. J. C. Berendsen, J. P. M. Postma, W. F. van Gunsteren, A. DiNola and J. R. Haak, *The Journal of Chemical Physics*, 1984, **81**, 3684-3690.
42. B. Hess, H. Bekker, H. J. C. Berendsen and J. G. E. M. Fraaije, *Journal of Computational Chemistry*, 1997, **18**, 1463-1472.
43. T. Darden, D. York and L. Pedersen, *The Journal of Chemical Physics*, 1993, **98**, 10089-10092.